Multiscale model for ultrashort pulsed parallel laser structuring—part II. The macroscale model

Christian Heinigk,[a,*] **T. Barthels**,[b] **W. Schulz**,[b] **and M. Nießen**[b]
[a]Rheinisch-Westfälisch Technische Hochschule Aachen University, Department Nichtlineare Dynamik der Laser-Fertigungsverfahren, Aachen, Germany
[b]Fraunhofer Institut für Lasertechnik, Aachen, Germany

Abstract. The increasing pixel density in displays demands high quality in the production of fine metal masks (FMMs). The production process of FMMs boils down to structuring tiny holes in thin metal sheets or foils. The manufacturing requirements of FMMs are high precision in terms of the hole geometry to let enough light escape from each diode and high productivity to produce the required amount. To achieve both objectives, high power ultrashort pulse (USP) lasers can be utilized. Because USP lasers fall short of the productivity requirements, they are combined with multibeam scanners. During production, the multibeam scanners deposit a lot of heat in the metal foil, which can ultimately yield temperature-induced distortions. To understand and finally avoid such distortions, a process simulation is sought. In a preceding study, the structuring of a single hole (the microscale) was investigated, but due to the large differences in the time and spatial scales involved, it was not feasible to simulate the production of the whole part (the macroscale). Within this treatise, a multiscale approach that takes into account the necessary information from the microscale to describe temperature-induced distortions on the macroscale is described. This approach targets laser ablation processes with pulse durations ranging from picoseconds up to nanoseconds provided the ablation is not melt-driven. First, a representative volume element (RVE) is generated from the results of the microscale model. Then, this RVE is utilized in the thermo-elastic structural mechanics simulation on the macroscale. The multiscale model is validated numerically against a hole-resolved computation, which shows good agreement. Naturally, the simulation is highly dependent on the microscale model, which in turn depends on the material properties. To handle material changes well, an experimental calibration has to be performed. This calibration is not part of this treatise, but it will be described in a future publication. In addition to the calibration process, the validation with experiments will be conducted in future research. Additionally, the authors envision the automation of the whole process, resulting in a first-time-right approach for the development of FMMs. Finally, the procedure might be extended to the requirements of other filtration purposes. [DOI: 10.1117/1.OE.61.9.095103]

Keywords: ultrashort pulsed laser; laser structuring; multiscale model; temperature-induced distortions; fine metal masks.

Paper 20220214G received Mar. 4, 2022; accepted for publication Aug. 18, 2022; published online Sep. 6, 2022.

1 Introduction

In today's consumer electronics, displays with ever-increasing pixel density are required. Within the production of such displays, fine metal masks (FMMs) with the highest quality have to be fabricated. Conventionally, the holes are etched into the metal foil; however, this process is reaching its limit as the defects accumulate for pixel densities around 600 PPI.[1] A technology that allows for such quality is high power ultrashort pulsed lasers.[2] The main reason for resorting to USP lasers is their ability to insert a lot of energy into the material without too much heating, which would destroy such thin foils.[2] To meet the productivity requirements, the laser can be combined with a multibeam scanner.[3] During the production of FMMs, it is important to avoid

*Address all correspondence to Christian Heinigk, christian.heinigk@nld.rwth-aachen.de

distortions or discoloration due to heat accumulation.[4] Therefore, process parameters and processing strategies that avoid such problems are sought.

Within this treatise, an extension to a simulation that computes the structuring of a single borehole, which has been explained in a prior publication,[5] is described. This time-consuming computation of a single borehole shape is used as the basis for a multiscale model with which the simulation of larger workpieces becomes feasible. The multiscale model consists of two scales.[6–10] First, the heat conduction and deformations are computed for a single borehole, the microscale. Second, the information on the microscale is collected in a representative volume element (RVE) with which the heat conduction and deformations of a whole workpiece, the macroscale, can be computed. The microscale model assumes pulse durations from femtoseconds up to nanoseconds as long as the ablation is not melt-driven.[11]

The unit cell, which is the computational domain in the microscale simulation, is the direct result of the simulation described in the prior publication.[5] Both the heat conduction and the thermo-elastic structural mechanics problems are discretized using a Bubnov–Galerkin method.[12–14] Averaging the results over the unit cell domain yields the material properties of the RVE.

On the macroscale, the computational domain is an FMM. It consists of two regions: one for a hole and one for the solid material. It is essential to use the RVE in the region that accounts for a hole and the ordinary material properties of the solid everywhere else. Again, a Bubnov–Galerkin scheme is employed to compute the temperature field and the distortions of the FMM.[12–14]

This treatise presents the multiscale approach using a simplified hole geometry. The homogenization of both models, the heat-conduction and the thermo-elasticity models, is performed using an asymptotic expansion in the scale variable as described in Ref. 6. To account for multi-beam scanners, the two-scale model can be adapted easily. This novel approach is capable of simulating the temperature field and elastic distortions occurring during the structuring of thin metal foils. Plastic strains and melt formation are not considered. The multiscale simulation computes accurate results in a fraction of the time compared with a fully-resolved simulation.

2 Multiscale Model

In a prior publication, the ablation of a structure with a single beam was explained.[5] This treatise extends the results to a multiscale model with which a periodic ablation pattern can be simulated for larger domains in a reasonable time.

The multiscale approach follows closely the works of Fish [8, Chapter I.3] or [6, Chapter 2.2]. To further reduce the computational demands, a residual-free method that allows for computing the microstructure off-line and in advance of the macroscale simulation was developed.

2.1 *Geometric Set-Up and Notation*

Hereafter, it is assumed that two length scales that differ in size enough to be separated exist, i.e., $0 < \zeta := \frac{\ell_\mathrm{f}}{\ell_\mathrm{c}} \ll 1$. Variables referring to a particular length scale are denoted with a subscript x_f for fine and x_c for coarse. Furthermore, the notation for functions that account for information on all scales uses a preceding superscript ${}^{\zeta}f$ and functions that are valid on the I'th scale use ${}^{I}f$. If not indicated otherwise, the variable x lives on the coarse scale, whereas the variable $y := x/\zeta$ lives on the fine scale. The computational domain is denoted as Ω with the boundary $\partial\Omega$. To account for different physical interactions with the environment, it is necessary to split this boundary into a Neumann part Γ_N and a Dirichlet part Γ_D, such that $\partial\Omega = \Gamma_N \cup \Gamma_D$ and $\Gamma_N \cap \Gamma_D = 0$ (c.f. Fig. 1). Analogously, the domain and boundaries for the unit cell are defined, except the symbol Θ is used. Whenever a distinction between Dirichlet and Neumann Boundary has to be made, Γ_D and Γ_N, respectively, are used.

The reason the artificial unit cell geometry [c.f. Fig. 1(a)] is used throughout this treatise is twofold. First, the computation of a realistic hole is already described in a prior publication,[5] and the geometries can be easily exchanged. Second, on the large scale, the difference between the artificial unit cell and a realistic unit cell is negligible.

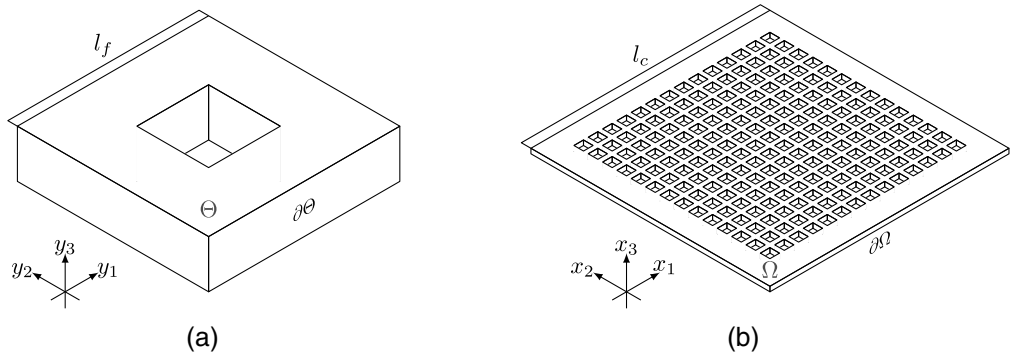

Fig. 1 (a) An artificial unit cell geometry is shown. In reality, the hole shape depends on the ablation strategy and the laser beam properties. (b) Displays a foil created using the unit cell in (a), although the hole sizes are emphasized.

In addition to the geometric notation, the Einstein summation convention is employed, i.e., repeated indices are summed. The derivative of a function $f(x_i)$ with respect to x_i is sometimes abbreviated with $\partial_{x_i} f$ to emphasize vector field operators such as the divergence. Averaged quantities are denoted with an overline, e.g., $\overline{x}$, vectors and matrices are highlighted in a boldface $\mathbf{x}$ and uppercase boldface $\mathbf{X}$, respectively. Finally, the subscript $f_{(i,x_j)}$ is used to denote the symmetrized gradient tensor entry, i.e.

$$f_{(i,x_j)} := \frac{1}{2}\left(\frac{\partial f_i}{\partial x_j} + \frac{\partial f_j}{\partial x_i}\right). \tag{1}$$

More complex geometries can be created using a level set function $\Phi(\mathbf{x}) : \mathbb{R}^n \to \mathbb{R}$. Such a level set function is the key result in the companion publication[5] wherein Φ is the solution that describes the ablation surface of a laser structuring process. A unit cell domain can be defined using this function on voxels by removing all elements that lie completely inside the ablated domain, i.e., for which $\Phi(\mathbf{x}) < 0$ holds. This can be seen in Fig. 2. The second result of the simulation described in Ref. 5 is the heat distribution after the ablation process is done. This heat distribution can be used as a volume source in Sec. 2.2.

2.2 *Two-Scale Heat Conduction*

The heat conduction equation for a material with specific density $\rho : {}^{\zeta}\Omega \to \mathbb{R}$, specific heat capacity $c_p : {}^{\zeta}\Omega \to \mathbb{R}$, and thermal conductivity $\lambda : {}^{\zeta}\Omega \to \mathbb{R}$ heated by a heat source $Q : {}^{\zeta}\Omega \to \mathbb{R}$ reads

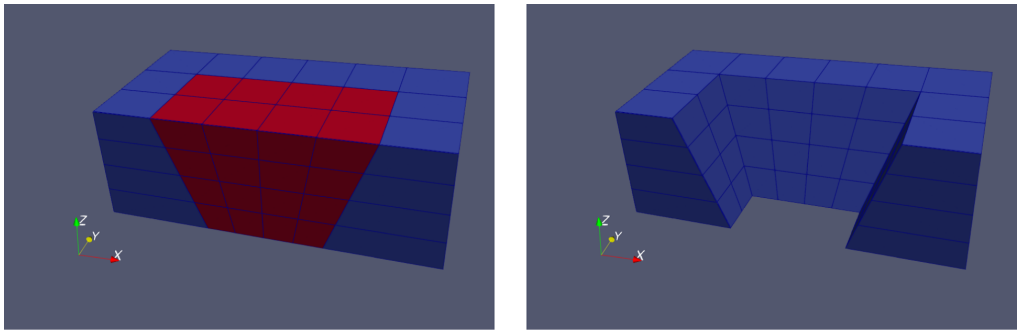

Fig. 2 A level set function can be used to mark elements that lie inside an ablated domain [c.f. Fig. 2(a)]. The final unit cell after removal of marked elements is shown in Fig. 2(b).

$$\begin{aligned}
\rho c_p \frac{\partial {}^{\zeta}T}{\partial t} + \frac{\partial {}^{\zeta}q_i}{\partial x_i} &= {}^{\zeta}Q \quad \text{in } {}^{\zeta}\Omega \\
{}^{\zeta}q_i &= -\lambda \frac{\partial {}^{\zeta}T}{\partial x_i} \quad \text{in } {}^{\zeta}\Omega \\
{}^{\zeta}q_i {}^{\zeta}n_i &= {}^{\zeta}q_N \quad \text{on } {}^{\zeta}\Gamma_N \\
{}^{\zeta}T &= {}^{\zeta}T_D \quad \text{on } {}^{\zeta}\Gamma_D.
\end{aligned} \tag{2}$$

Herein, n_i, refers to the i'th entry of the outward pointing unit normal n, e.g. $n = (n_1, n_2, n_3)^T$ in three dimensions. The solution to this problem is the temperature field $T : {}^{\zeta}\Omega \to \mathbb{R}$. In general, the functions depend on both the coarse and fine scales, but for the density and the specific heat capacity a dependence on the fine scale variable only is assumed, i.e., $\rho := \rho(\mathbf{y})$ and $c_p := c_p(\mathbf{y})$.

Now, an ansatz function for the temperature is defined by means of an asymptotic expansion[15] using the scale ζ, which reads

$${}^{\zeta}T(\mathbf{x}) := T(\mathbf{x}, \mathbf{y}) = \zeta^{00}T(\mathbf{x}, \mathbf{y}) + \zeta^{11}T(\mathbf{x}, \mathbf{y}) + O(\zeta^2) + \cdots . \tag{3}$$

Note that terms of order 2 and above have been omitted as they do not contribute significantly to the temperature due to the condition $\zeta \ll 1$. Fourier's law in Eq. (2) relates the temperature gradient to the heat flux; therefore, the spatial derivative of Eq. (3) is taken. Rearranging the terms in accordance to the order of ζ yields

$$\frac{\partial {}^{\zeta}T}{\partial x_i}(\mathbf{x}) = \frac{\partial T}{\partial x_i}(\mathbf{x}, \mathbf{y}) = \zeta^{-10}T(\mathbf{x}, \mathbf{y}) + \zeta^0 \left(\frac{\partial^0 T}{\partial x_i}(\mathbf{x}, \mathbf{y}) + \frac{\partial^1 T}{\partial y_i}(\mathbf{x}, \mathbf{y}) \right) + \zeta^1 \frac{\partial^1 T}{\partial x_i}(\mathbf{x}, \mathbf{y}) \quad + O(\zeta^2) + \cdots . \tag{4}$$

Again, higher-order terms are omitted in the two-scale formulation. Multiplying this equation with the negative thermal conductivity and a comparison of the coefficients results in

$$\begin{aligned}
-\lambda \frac{\partial T}{\partial x_i}(\mathbf{x}, \mathbf{y}) &= -\zeta^{-1}\lambda^0 T(\mathbf{x}, \mathbf{y}) - \zeta^0 \lambda \left(\frac{\partial^0 T}{\partial x_i}(\mathbf{x}, \mathbf{y}) + \frac{\partial^1 T}{\partial y_i}(\mathbf{x}, \mathbf{y}) \right) - \zeta^1 \lambda \frac{\partial^1 T}{\partial x_i}(\mathbf{x}, \mathbf{y}) - O(\zeta^2) - \cdots \\
q_i(\mathbf{x}) &= \zeta^{-1-1} q_i(\mathbf{x}, \mathbf{y}) + \zeta^{00} q_i(\mathbf{x}, \mathbf{y}) + \zeta^{11} q_i(\mathbf{x}, \mathbf{y}) + O(\zeta^2) + \cdots .
\end{aligned} \tag{5}$$

The divergence of the heat flux is needed, too. Taking the derivative with respect to the i'th space component and sorting in ascending orders of ζ yields

$$\frac{\partial q_i}{\partial x_i} = \zeta^{-2} \frac{\partial^{-1} q_i}{\partial y_i} + \zeta^{-1} \left(\frac{\partial^{-1} q_i}{\partial x_i} + \frac{\partial^0 q_i}{\partial y_i} \right) + \zeta^0 \left(\frac{\partial^0 q_i}{\partial x_i} + \frac{\partial^1 q_i}{\partial y_i} \right) + \zeta^1 \left(\frac{\partial^1 q_i}{\partial x_i} + \frac{\partial^2 q_i}{\partial y_i} \right) + O(\zeta^2) + \cdots . \tag{6}$$

Here, the functions' arguments are dropped for brevity. Inserting the ansatz functions—Eq. (3) for the temperature and Eq. (5) for the heat flux—in the energy balance in Eq. (2) gives

$$\rho c_p \frac{\partial ({}^0T + \zeta^1 T)}{\partial t} + \zeta^{-2} \frac{\partial^{-1} q_i}{\partial y_i} + \zeta^{-1} \left(\frac{\partial^{-1} q_i}{\partial x_i} + \frac{\partial^0 q_i}{\partial y_i} \right) + \zeta^0 \left(\frac{\partial^0 q_i}{\partial x_i} + \frac{\partial^1 q_i}{\partial y_i} \right) + O(\zeta) + \cdots = {}^{\zeta}Q. \tag{7}$$

Note the truncation at $O(\zeta)$. The terms are now rearranged and collected in orders of ζ. More rigorously, Eq. (7) is multiplied by ζ^2 first, then by ζ^1, which, after taking the limit $\zeta \to 0^+$, yields a system of three equations:

$$O(\zeta^{-2}): \ \frac{\partial^{-1} q_i}{\partial y_i} = 0, \tag{8}$$

$$O(\zeta^{-1}): \ \frac{\partial^{-1} q_i}{\partial x_i} + \frac{\partial^0 q_i}{\partial y_i} = 0, \tag{9}$$

$$O(\zeta^0)\colon \rho c_p \frac{\partial({}^0T + \zeta^1 T)}{\partial t} + \frac{\partial^0 q_i}{\partial x_i} + \frac{\partial^1 q_i}{\partial y_i} = {}^{\zeta}Q. \tag{10}$$

Henceforth, it is assumed that the heat source ${}^{\zeta}Q$ and the boundary conditions ${}^{\zeta}q_N$ and ${}^{\zeta}T_D$ in Eq. (2) depend on the coarse scale only. The system still needs closure.

Multiplying Eq. (8) with ${}^0T$ and integrating over the unit cell gives

$$\int_{\Theta} {}^0T \frac{\partial^{-1} q_i}{\partial y_i} \mathrm{d}y = 0. \tag{11}$$

which, after applying the product rule of the divergence operator and the divergence theorem, reads

$$\int_{\partial\Theta} {}^0T^{-1} q_i n_i \mathrm{d}y - \int_{\Theta} \frac{\partial^0 T}{\partial y_i} {}^{-1}q_i \mathrm{d}y = 0. \tag{12}$$

Because periodic boundary conditions are employed on the unit cell, the temperature and heat flux on opposite points of the boundary are equal, but the normal points in exactly opposite directions, and therefore, the boundary integral vanishes. Inserting the corresponding coefficient from the ansatz in Fourier's law Eq. (5) gives

$$\int_{\Theta} \frac{\partial^0 T}{\partial y_i} \lambda \frac{\partial^0 T}{\partial y_i} \mathrm{d}y = 0. \tag{13}$$

From $\lambda > 0$ follows $\frac{\partial^0 T}{\partial y_i} = 0$, which implies an independence on the fine scale, i.e., ${}^0T \coloneqq {}^0T(\mathbf{x})$.

Through Eq. (5), this also holds for the corresponding part of the heat flux

$${}^{-1}q_i = -\lambda \frac{\partial^0 T}{\partial y_i} = 0. \tag{14}$$

Now, Eq. (9) is considered. Inserting Eq. (14) results in

$$\frac{\partial^0 q_i}{\partial y_i} = 0. \tag{15}$$

Again, the expression for the corresponding part of the heat flux from Eq. (5) can be inserted, which yields

$$\frac{\partial}{\partial y_i}\left(\lambda\left(\frac{\partial^0 T}{\partial x_i} + \frac{\partial^1 T}{\partial y_i}\right)\right) = 0. \tag{16}$$

Using the ansatz ${}^1T(\mathbf{x},\mathbf{y}) = H_j(\mathbf{y})\partial_{x_j}{}^0T(\mathbf{x})$ and factoring out $\partial_{x_j}{}^0T(\mathbf{x})$ gives

$$\frac{\partial}{\partial y_i}\left(\lambda\left(\delta_{ij} + \frac{\partial H_j(\mathbf{y})}{\partial y_i}\right)\right) = 0, \tag{17}$$

with the temperature influence function $H_j\colon {}^{\zeta}\Omega \to \mathbb{R} \in C^0(\Theta)$ and the usual Dirac delta δ_{ij}. Boundary conditions depend on the coarse scale only, and the fact that ${}^0T$ already accounts for all information on the boundary, the fine scale problem reads

Find $H_j(\mathbf{y})$, such that

$$\begin{aligned} \frac{\partial}{\partial y_i}\left(\lambda\left(\delta_{ij} + \frac{\partial H_j(\mathbf{y})}{\partial y_i}\right)\right) &= 0, \quad \text{in } \Theta \\ H_j(\mathbf{y}) &= 0 \quad \text{on } \partial\Theta. \end{aligned} \tag{18}$$

With the current information, the temperature ansatz Eq. (3) is given as

$$ {}^{\zeta}T(\mathbf{x}) = T(\mathbf{x},\mathbf{y}) \approx {}^{0}T(\mathbf{x}) + \zeta^{1}H_j(\mathbf{y})\frac{\partial^0 T(\mathbf{x})}{\partial x_j}. \tag{19} $$

On the coarse scale, the temperature is defined to be the multiscale temperature averaged over the unit cell:

$$ \begin{aligned} {}^{c}T(\mathbf{x}) &= \frac{1}{\mathrm{vol}(\Theta)}\int_\Theta {}^{\zeta}T(\mathbf{x})\mathrm{d}y \approx \frac{1}{\mathrm{vol}(\Theta)}\int_\Theta {}^{0}T(\mathbf{x}) + \zeta^{1}H_j(\mathbf{y})\frac{\partial^0 T(\mathbf{x})}{\partial x_j}\mathrm{d}y \\ &= \frac{{}^{0}T(\mathbf{x})}{\mathrm{vol}(\Theta)}\int_\Theta \mathrm{d}y + \frac{\zeta^{1}\partial_{x_j}{}^{0}T(\mathbf{x})}{\mathrm{vol}(\Theta)}\int_\Theta H_j(\mathbf{y})\mathrm{d}y, \end{aligned} \tag{20} $$

and thus, ${}^{c}T = {}^{0}T$, if and only if $\int_\Theta H_j(\mathbf{y})\mathrm{d}y = 0$.

Inserting the corresponding relation of the heat flux ansatz Eq. (5) into Eq. (17) yields

$$ \begin{aligned} {}^{0}q_i &= -\Lambda_{ij}\frac{\partial^0 T}{\partial x_j} \\ \Lambda_{ij} &:= \lambda\left(\delta_{ij} + \frac{\partial H_j}{\partial y_i}\right), \end{aligned} \tag{21} $$

in which Λ_{ij} is termed the heat flux influence function.

Finally, the zeroth-order terms of ζ Eq. (10) are averaged over the unit cell, resulting in

$$ \frac{1}{\mathrm{vol}(\Theta)}\int_\Theta \rho c_p\frac{\partial^0 T}{\partial t} + \frac{\partial^0 q_i}{\partial x_i}\mathrm{d}y + \frac{1}{\mathrm{vol}(\Theta)}\int_\Theta \frac{\partial^1 q_i}{\partial y_i}\mathrm{d}y - \frac{1}{\mathrm{vol}(\Theta)}\int_\Theta {}^{\zeta}Q\mathrm{d}y = 0. \tag{22} $$

Rearranging the first integral and applying the divergence theorem to the second gives

$$ \frac{\partial^0 T}{\partial t}\frac{1}{\mathrm{vol}(\Theta)}\int_\Theta \rho c_p\mathrm{d}y + \frac{\partial}{\partial x_i}\left(\frac{1}{\mathrm{vol}(\Theta)}\int_\Theta {}^{0}q_i\mathrm{d}y\right) + \frac{1}{\mathrm{vol}(\Theta)}\int_{\partial\Theta} {}^{1}q_i n_i\mathrm{d}y - \frac{1}{\mathrm{vol}(\Theta)}\int_\Theta {}^{\zeta}Q\mathrm{d}y = 0, \tag{23} $$

wherein the boundary integral vanishes due to ${}^{1}q_i = -\lambda\partial_{x_i}{}^{1}T = -\lambda H_j\partial_{x_j}{}^{0}T$ and $H_j = 0$ for $y \in \partial\Theta$, resulting in

$$ \frac{\partial^0 T}{\partial t}\frac{1}{\mathrm{vol}(\Theta)}\int_\Theta \rho c_p\mathrm{d}y + \frac{\partial}{\partial x_i}\left(\frac{1}{\mathrm{vol}(\Theta)}\int_\Theta {}^{0}q_i\mathrm{d}y\right) - \frac{1}{\mathrm{vol}(\Theta)}\int_\Theta {}^{\zeta}Q\mathrm{d}y = 0. \tag{24} $$

Henceforth, averaged quantities are denoted with a horizontal line above them, e.g., $\overline{\rho c_p} := \frac{1}{\mathrm{vol}(\Theta)}\int_\Theta \rho c_p\mathrm{d}y$. With this notation in place, the coarse scale heat conduction reads

$$ \frac{\partial^0 T}{\partial t}\overline{\rho c_p} + \frac{\partial \overline{{}^{0}q_i}}{\partial x_i} - \overline{{}^{\zeta}Q} = 0. \tag{25} $$

In summary, two problems have to be solved: one on the fine scale and one on the coarse scale. The fine scale problem reads

Find $H_j(\mathbf{y})$, such that

$$ \frac{\partial}{\partial y_i}\left(\lambda\left(\delta_{ij} + \frac{\partial H_j}{\partial y_i}\right)\right) = 0, \quad \text{in } \Theta \quad H_j = 0, \quad \text{on } \partial\Theta. \tag{26} $$

From the solution, the heat flux influence function Λ_{ij} can be computed using Eq. (21). The coarse scale problem is then defined as

Find ${}^0T(\mathbf{x})$, such that

$$\begin{aligned}\overline{\rho c_p}\frac{\partial^0 T}{\partial t}-\frac{\partial}{\partial x_i}\left(\overline{\Lambda_{ij}}\frac{\partial^0 T}{\partial x_j}\right)&=\overline{Q}, \quad \text{in } \Omega\times[0,t_{\max}]\\ {}^0T&=\overline{T}_0, \quad \text{in } \Omega\times\{0\}\\ \overline{\Lambda_{ij}}\frac{\partial^0 T}{\partial x_j}n_i&=q_{\mathrm{N}}, \quad \text{on } \partial\Omega\,.\end{aligned} \tag{27}$$

The overall temperature function ${}^\zeta T$ can then be constructed as

$${}^\zeta T(\mathbf{x},\mathbf{y})\approx {}^0T+\zeta H_j(\mathbf{y})\frac{\partial^0 T(\mathbf{x})}{\partial x_j}. \tag{28}$$

2.3 *Thermo-Elastic Deformations*

To define the multiscale structural-mechanics equations, which describe the deformation of a solid under volume and thermal loading conditions, a few functions have to be introduced. For an n-dimensional domain, the displacement is denoted $u:{}^\zeta\Omega\to\mathbb{R}^n$. Note that it does not depend on time. The body forces acting on the work piece are written as $b:{}^\zeta\Omega\to\mathbb{R}^n$. The notations for strains and stresses resulting from the loads read $\epsilon:{}^\zeta\Omega\to\mathbb{R}^{n\times n}$ and $\sigma:{}^\zeta\Omega\to\mathbb{R}^{n\times n}$, respectively. They are related through the stiffness tensor $C\in\mathbb{R}^{n\times n\times n\times n}$. Using these definitions, the static equilibrium of stresses in index notation is given as

$$\begin{aligned}\frac{\partial {}^\zeta\sigma_{ij}}{\partial x_j}+{}^\zeta b_i&=0, \quad \text{in } {}^\zeta\Omega\\ {}^\zeta\sigma_{ij}&={}^\zeta C_{ijkl}\,{}^\zeta\epsilon^{\mathrm{el}}_{kl}, \quad \text{in } {}^\zeta\Omega\\ {}^\zeta\sigma_{ij}n_j&={}^\zeta\overline{t}_i, \quad \text{on } {}^\zeta\Gamma_N\\ {}^\zeta u_i&={}^\zeta\overline{u}_i, \quad \text{on } {}^\zeta\Gamma_D.\end{aligned} \tag{29}$$

Herein, the total ϵ^{tot} strain is the sum of the elastic ϵ^{el}, plastic ϵ^{pl}, and thermal ϵ^{th} strains:

$$\begin{aligned}{}^\zeta\epsilon^{\mathrm{tot}}_{kl}&={}^\zeta\epsilon^{\mathrm{el}}_{kl}+{}^\zeta\epsilon^{\mathrm{th}}_{kl}, \quad \text{in } {}^\zeta\Omega\\ {}^\zeta\epsilon^{\mathrm{tot}}_{kl}&=\frac{1}{2}\left(\frac{\partial {}^\zeta u_k}{\partial x_l}+\frac{\partial {}^\zeta u_l}{\partial x_k}\right), \quad \text{in } {}^\zeta\Omega\\ {}^\zeta\epsilon^{\mathrm{th}}_{kl}&=-\alpha\Delta {}^\zeta T\delta_{kl}, \quad \text{in } {}^\zeta\Omega.\end{aligned} \tag{30}$$

The stiffness tensor obeys a symmetry condition

$${}^\zeta C_{ijkl}={}^\zeta C_{jikl}={}^\zeta C_{ijlk}={}^\zeta C_{klij}, \tag{31}$$

and is positive in the sense that

$$\exists\ c>0\colon {}^\zeta C_{ijkl}n_{ij}n_{kl}\geq cn_{ij}n_{ij}, \quad \forall\ n_{ij}=n_{ji}. \tag{32}$$

Analogously to the two-scale heat conduction in Sec. 2.2, the asymptotic ansatz for the displacement is defined to be

$${}^\zeta u_i(\mathbf{x}) \coloneqq u_i(\mathbf{x},\mathbf{y})={}^0u_i(\mathbf{x},\mathbf{y})+\zeta^1 u_i(\mathbf{x},\mathbf{y})+\zeta^{22}u_i(\mathbf{x},\mathbf{y})+O(\zeta^3)+\cdots\,. \tag{33}$$

From Eq. (29), it is obvious that the derivative is required, too. Taking the derivative with respect to x_j, applying the chain rule, and sorting in ascending order of ζ yields

$$\frac{\partial u_i}{\partial x_j}(\mathbf{x},\mathbf{y}) = \zeta^{-1}\frac{\partial^0 u_i}{\partial y_j}(\mathbf{x},\mathbf{y}) + \zeta^0\left(\frac{\partial^0 u_i}{\partial x_j}(\mathbf{x},\mathbf{y}) + \frac{\partial^1 u_i}{\partial y_j}(\mathbf{x},\mathbf{y})\right) + \zeta^1\left(\frac{\partial^1 u_i}{\partial x_j}(\mathbf{x},\mathbf{y}) + \frac{\partial^2 u_i}{\partial y_j}(\mathbf{x},\mathbf{y})\right) + \zeta^2\left(\frac{\partial^2 u_i}{\partial x_j}(\mathbf{x},\mathbf{y}) + \frac{\partial^3 u_i}{\partial y_j}(\mathbf{x},\mathbf{y})\right) + O(\zeta^3) + \cdots = \zeta^{-1}\frac{\partial^0 u_i}{\partial y_j}(\mathbf{x},\mathbf{y}) + \sum_{s=0}^{2}\zeta^s\left(\frac{\partial^s u_i}{\partial x_j}(\mathbf{x},\mathbf{y}) + \frac{\partial^{s+1} u_i}{\partial y_j}(\mathbf{x},\mathbf{y})\right) + O(\zeta^3) + \cdots . \tag{34}$$

Inserting into the strain–displacement relation in Eq. (30) gives

$$\epsilon_{ij}^{\mathrm{el}}(\mathbf{x},\mathbf{y}) = \zeta^{-1}\frac{1}{2}\left(\frac{\partial^0 u_i}{\partial y_j} + \frac{\partial^0 u_j}{\partial y_i}\right) + \sum_{s=0}^{2}\zeta^s\frac{1}{2}\left(\frac{\partial^s u_i}{\partial x_j} + \frac{\partial^s u_i}{\partial x_j} + \frac{\partial^{s+1} u_i}{\partial y_j} + \frac{\partial^{s+1} u_i}{\partial y_j}\right) + O(\zeta^3) + \cdots = \zeta^{-1-1}\epsilon_{ij}^{\mathrm{el}} + \sum_{s=0}^{2}\zeta^{ss}\epsilon_{ij}^{\mathrm{el}} + O(\zeta^3) + \cdots . \tag{35}$$

Assuming the stiffness tensor is independent of the coarse scale, i.e., $C_{ijkl}(\mathbf{x},\mathbf{y}) \coloneqq C_{ijkl}(\mathbf{y})$, and inserting the ansatz for the elastic strain Eq. (35) into the stress–strain relation Eq. (29) results in the two-scale ansatz for the stress

$$\sigma_{ij}(\mathbf{x},\mathbf{y}) = C_{ijkl}(\mathbf{y})\left(\zeta^{-1-1}\varepsilon_{ij}^{\mathrm{el}} + \sum_{s=0}^{2}\zeta^{ss}\varepsilon_{ij}^{\mathrm{el}}\right) + O(\zeta^3) + \cdots = \zeta^{-1-1}\sigma_{ij} + \sum_{s=0}^{2}\zeta^{ss}\sigma_{ij} + O(\zeta^3) + \cdots . \tag{36}$$

Again, the derivative of the stress with respect to space is needed as it appears in Eq. (29). Thus, inserting the derivative, which reads

$$\frac{\partial \sigma_{ij}}{\partial x_j}(\mathbf{x},\mathbf{y}) = \zeta^{-2}\frac{\partial^{-1}\sigma_{ij}}{\partial y_j} + \zeta^{-1}\left(\frac{\partial^{-1}\sigma_{ij}}{\partial x_j} + \frac{\partial^0 \sigma_{ij}}{\partial y_j}\right) + \zeta^0\left(\frac{\partial^0 \sigma_{ij}}{\partial x_j} + \frac{\partial^1 \sigma_{ij}}{\partial y_j}\right) + O(\zeta), \tag{37}$$

in the stress balance and sorting in ascending order of ζ yields

$$\zeta^{-2}\frac{\partial^{-1}\sigma_{ij}}{\partial y_j} + \zeta^{-1}\left(\frac{\partial^{-1}\sigma_{ij}}{\partial x_j} + \frac{\partial^0 \sigma_{ij}}{\partial y_j}\right) + \zeta^0\left(\frac{\partial^0 \sigma_{ij}}{\partial x_j} + \frac{\partial^1 \sigma_{ij}}{\partial y_j} + {}^{\zeta}b_i\right) + O(\zeta) = 0. \tag{38}$$

Analogously to the derivation of the two-scale heat conduction problem, the leading order terms of the stress balance are obtained by multiplication with ζ^2 and ζ, respectively, and taking the limit $\zeta \to 0$:

$$O(\zeta^{-2}):\ \frac{\partial^{-1}\sigma_{ij}}{\partial y_j} = 0, \tag{39}$$

$$O(\zeta^{-1}):\ \frac{\partial^{-1}\sigma_{ij}}{\partial x_j} + \frac{\partial^0 \sigma_{ij}}{\partial y_j} = 0, \tag{40}$$

$$O(\zeta^0):\ \frac{\partial^0 \sigma_{ij}}{\partial x_j} + \frac{\partial^1 \sigma_{ij}}{\partial y_j} + {}^{\zeta}b_i = 0. \tag{41}$$

It is, hereafter, assumed that the body force depends on the fine scale only ${}^{\zeta}b_i(\mathbf{x}) \coloneqq b_i(\mathbf{y})$, and the boundary conditions in Eq. (29) are coarse scale functions ${}^{\zeta}\overline{t}_i(\mathbf{x}) \coloneqq \overline{t}_i(\mathbf{x})$ and ${}^{\zeta}\overline{u}_i(\mathbf{x}) \coloneqq \overline{u}_i(\mathbf{x})$. For closure, the moments are computed for each order. Therefore, multiplying Eq. (39) by ${}^0u_i$ and integrating over the unit cell gives

$$\int_{\Theta} {}^{0}u_i \frac{\partial^{-1}\sigma_{ij}}{\partial y_j} \mathrm{d}y = 0. \tag{42}$$

Using the product rule of divergence and the divergence theorem, as well as noting that the resulting boundary integral vanishes due to periodicity of both integrands and opposing normals, results in

$$\int_{\Theta} \frac{\partial^{0}u_i}{\partial y_j} {}^{-1}\sigma_{ij} \mathrm{d}y = 0. \tag{43}$$

Inserting the definitions of ${}^{-1}\sigma_{ij}$ and ${}^{-1}\epsilon_{ij}^{\mathrm{el}}$ from Eqs. (36) and (35), respectively, yields

$$\int_{\Theta} \frac{\partial^{0}u_i}{\partial y_j} C_{ijkl} \frac{1}{2}\left(\frac{\partial^{0}u_k}{\partial x_l} + \frac{\partial^{0}u_l}{\partial x_k}\right) \mathrm{d}y = 0. \tag{44}$$

From the symmetry and positiveness of the stiffness tensor C, it can be inferred that

$$\frac{\partial^{0}u_i}{\partial x_j} = 0, \tag{45}$$

and, with Eqs. (36) and (35),

$${}^{-1}\sigma_{ij} = 0. \tag{46}$$

Inserting Eq. (46) into Eq. (40) gives

$$\frac{\partial^{0}\sigma_{ij}}{\partial y_j} = 0, \tag{47}$$

which, with the definition of ${}^{0}\sigma_{ij}$ from Eq. (36) and ${}^{0}\epsilon_{\mathrm{ij}}$ from Eq. (35), results in

$$\frac{\partial}{\partial y_j}\left(C_{ijkl}\left(\frac{1}{2}\left(\frac{\partial^{0}u_k}{\partial x_l} + \frac{\partial^{0}u_l}{\partial x_k}\right) + \frac{1}{2}\left(\frac{\partial^{1}u_k}{\partial x_l} + \frac{\partial^{1}u_l}{\partial x_k}\right)\right)\right) = 0. \tag{48}$$

This shows a direct dependence between the displacement of the zeroth and first scale. Hence, the separation of variables ansatz

$${}^{1}u_i := {}^{mn}H_i(\mathbf{y}) \frac{1}{2}\left(\frac{\partial^{0}u_m}{\partial x_n} + \frac{\partial^{0}u_n}{\partial x_m}\right), \tag{49}$$

with the first-order displacement influence function H, is employed. It is assumed that the influence function is symmetric ${}^{mn}H_i = {}^{mn}H_i$, locally periodic, and continuous $H \in C^0(\Omega)$. Inserting the ansatz in Eq. (48) yields

$$\frac{\partial}{\partial y_j}(C_{ijkl}({}^{0}u_{(k,x_l)} + {}^{mn}H^{0}_{(k,y_l)}u_{(m,x_n)})) = 0, \tag{50}$$

and after factoring out ${}^{0}u_{(m,x_n)}$

$$\frac{\partial}{\partial y_j}(C_{ijkl}(I_{klmn} + {}^{mn}H_{(k,y_l)}))^{0}u_{(m,x_n)} = 0, \tag{51}$$

with the definition $I_{klmn} := \frac{1}{2}(\delta_{km}\delta_{ln} + \delta_{lm}\delta_{kn})$. Because ${}^{0}u_{(m,x_n)}$ is arbitrary, it is required that

$$\frac{\partial}{\partial y_j}(C_{ijkl}(I_{klmn} + {}^{mn}H_{(k,y_l)})) = 0. \tag{52}$$

To have a well-defined problem in the sense of Hadamard, an additional condition is needed. In the literature,[6–8] two conditions are reported:

1. ${}^{mn}H_k(\mathbf{y}) = 0,$ on $\partial\Theta_{\text{vert}}$, and
2. $\int_\Theta {}^{mn}H_k(\mathbf{y})\mathrm{d}y = 0,$ in Θ.

Herein, $\partial\Theta_{\text{vert}}$ denotes the vertices of the unit cell boundary $\partial\Theta$. As always, each has advantages over the other. Although condition 1 is simpler to implement, condition 2 associates ${}^0u_i(\mathbf{x})$ with the average displacement ${}^{\text{c}}u_i$ through

$$ {}^{\text{c}}u(x) := \frac{1}{\text{vol}(\Theta)} \int_\Theta {}^{\zeta}u(x,y)\mathrm{d}y. \tag{53} $$

With the fine-scale displacement ansatz, the overall displacement function reads

$$ u_i(\mathbf{x},\mathbf{y}) = {}^0u_i(\mathbf{x}) + \zeta^{m\,n}H_i(\mathbf{y}){}^0u_{(m,x_n)}(\mathbf{x}) + O(\zeta^2), \tag{54} $$

which can be inserted into Eq. (53)

$$ \begin{aligned} {}^{\text{c}}u_i(\mathbf{x}) &:= \frac{1}{\text{vol}(\Theta)} \int_\Theta {}^0u_i(\mathbf{x}) + \zeta^{mn}H_i(\mathbf{y}){}^0u_{(m,x_n)}(\mathbf{x}) + O(\zeta^2)\mathrm{d}y \\ &= {}^0u_{(m,x_n)}(\mathbf{x}) \frac{1}{\text{vol}(\Theta)} \int_\Theta 1\mathrm{d}y \\ &= {}^0u(\mathbf{x}). \end{aligned} \tag{55} $$

Within this treatise, condition 2 has been applied. From this, the leading order strain is given as

$$ \begin{aligned} {}^0\epsilon_{ij}^{tot} &= {}^0u_{(i,x_j)} + {}^1u_{(i,x_j)} \\ &= (I_{ijkl} + {}^{mn}H_{(k,y_l)}(y)){}^0u_{(m,x_n)} \\ &= E_{mnkl}{}^0u_{(m,x_n)} \\ &= :{}^f\epsilon_{\text{kl}}^{tot}(x,y), \end{aligned} \tag{56} $$

with the strain influence function $E_{mnkl} := I_{ijkl} + {}^{mn}H_{(k,y_l)}(y)$ and the fine-scale total strain ${}^f\epsilon^{\text{tot}}$. Averaging the fine-scale total strain over the unit cell yields the coarse-scale total strain

$$ {}^{\text{c}}\epsilon_{mn}^{tot}(x) := \frac{1}{\text{vol}(\Theta)} \int_\Theta {}^f\epsilon_{mn}^{tot}(x,y)\mathrm{d}y \quad = {}^0u_{(m,x_n)}. \tag{57} $$

Herein, the integral vanishes due to the divergence identity, the divergence theorem, and the local periodicity of the displacement influence function. With this, the coarse scale total strain is given as

$$ {}^f\epsilon_{kl}^{tot}(x,y) := E_{mnkl}(y){}^{\text{c}}\epsilon_{\text{mn}}^{tot}(x). \tag{58} $$

The leading stress is computed according to

$$ {}^0\sigma_{ij}(x,y) := \Sigma_{ijmn}(y){}^{\text{c}}\epsilon_{mn}^{\text{tot}}(x) = :{}^f\sigma_{ij}(x,y), \tag{59} $$

with the stress influence function $\Sigma_{ijmn} := C_{ijkl}E_{klmn}$.

Finally, the highest order, i.e., Eq. (41), averaged over the unit cell reads

$$\frac{1}{\mathrm{vol}(\Theta)}\int_\Theta \frac{\partial^0 \sigma_{ij}}{\partial y_j}+\frac{\partial^1 u_{ij}}{\partial y_j}+{}^{\zeta}b_i \mathrm{d}y = 0$$
$$\frac{1}{\mathrm{vol}(\Theta)}\int_\Theta \frac{\partial^0 \sigma_{ij}}{\partial y_j}+{}^{\zeta}b_i \mathrm{d}y = 0. \tag{60}$$

Herein, the second term vanishes after applying the divergence theorem and due to local periodicity. Inserting the stress–strain and strain–displacement relations for the respective scale yields

$$\frac{1}{\mathrm{vol}(\Theta)}\int_\Theta C_{ijkl}E_{klmn}(\mathbf{y})\mathrm{d}y \frac{\partial}{\partial x_j}{}^0 u_{(m,x_n)}(\mathbf{x})) + \frac{1}{\mathrm{vol}(\Theta)}\int_\Theta {}^{\zeta}b_i \mathrm{d}y = 0$$
$${}^{c}C_{ijmn}\frac{\partial}{\partial x_j}({}^{c}\epsilon^{\mathrm{tot}}_{mn}) + {}^{c}b_i = 0$$
$$\frac{\partial {}^{c}\sigma_{ij}}{\partial x_j} + {}^{c}b_i = 0, \tag{61}$$

with the according definitions of ${}^{c}C_{ijmn}$ and ${}^{c}\sigma_{ij}$.

In summary, on the fine scale, the problem reads

Find ${}^{mn}H_i(\mathbf{y})$, such that

$$\frac{\partial}{\partial y_j}(C_{ijkl}({}^{mn}H_{(k,y_l)} + I_{klmn})) = 0, \quad \text{in } \Theta$$
$$\int_\Theta {}^{mn}H_i(y)\mathrm{d}y = 0, \quad \text{in } \Theta$$
$${}^{mn}H_i(y) = {}^{mn}H_i(y+l), \quad \text{on } \partial\Theta, \tag{62}$$

where l is chosen, such that $y + l$ is the point on the boundary opposite of y. The problem on the coarse scale is

Find ${}^{c}u_i(\mathbf{x})$, such that

$$\frac{\partial {}^{c}\sigma_{ij}}{\partial x_j} + {}^{c}b_i = 0, \quad \text{in } \Omega$$
$${}^{c}\sigma_{ij} = {}^{c}C_{ijmn}{}^{c}\epsilon^{\mathrm{tot}}_{\mathrm{mn}}, \quad \text{in } \Omega$$
$${}^{c}u_i = {}^{c}\overline{u}_i, \quad \text{on } \Gamma_D$$
$${}^{c}\sigma_{ij}n_j = {}^{c}\overline{t}_i, \quad \text{on } \Gamma_N. \tag{63}$$

Finally, the overall displacements can be recovered with

$$u_i(\mathbf{x},\mathbf{y}) = {}^0u_i(\mathbf{x}) + \zeta^{mn}H_k(\mathbf{y}){}^0u_{(m,x_n)}(\mathbf{x}). \tag{64}$$

3 Weak Formulation

To solve the aforementioned systems numerically, a Galerkin method is applied in the space dimension. The time discretization is performed using the Euler method. First, the two-scale heat conduction is explained, and second, the thermo-elasticity problem is discussed.

3.1 *Two-Scale Heat Conduction*

Remembering the equation for the temperature influence function, i.e., Eq. (26), and choosing trial and test functions from the Hilbert space $\phi, \varphi \in \mathcal{H}^1_0(\Omega)$, containing functions vanishing on the boundary, the temperature influence function can be approximated within this space to read

$$H_j(\mathbf{y}) \approx \hat{H}_{jk}\phi_k(\mathbf{y}), \quad k = 1, \ldots, K. \tag{65}$$

Multiplying Eq. (26) by arbitrary test functions and integrating over the unit cell yields

$$\int_\Theta \frac{\partial}{\partial y_i}\left(\lambda\left(\delta_{ij} + \frac{\partial \hat{H}_{jk}\phi_k}{\partial y_i}\right)\right)\varphi_l \mathrm{d}y = 0, \quad \forall\, \varphi_l, \quad l = 1, \ldots, L. \tag{66}$$

Constant terms can be factored out and brought to the right side. Using the product rule for the divergence operator and applying the divergence theorem gives

$$-\int_\Theta \lambda \frac{\partial}{\partial y_i}(\hat{H}_{jk}\phi_k)\frac{\partial \varphi_l}{\partial y_i}\mathrm{d}y = -\int_\Theta \frac{\partial}{\partial y_i}(\lambda\delta_{ij}\varphi_l)\mathrm{d}y. \tag{67}$$

Note that the boundary integral vanishes due to vanishing test functions. With the definition of a system matrix $A \in \mathbb{R}^{L\times K}$ and a thermal load vector $\mathbf{b}_j \in \mathbb{R}^L$, such that

$$\begin{aligned} A_{lk} &\coloneqq \int_\Theta \lambda \frac{\partial \phi_k}{\partial y_i}\frac{\partial \varphi_l}{\partial y_i}\mathrm{d}y, \\ b_l &\coloneqq \int_\Theta \frac{\partial}{\partial y_i}(\lambda\delta_{ij})\varphi_l \mathrm{d}y. \end{aligned} \tag{68}$$

The problem can be written in matrix form, i.e.

$$A\hat{\mathbf{H}}_j = \mathbf{b}_j. \tag{69}$$

Solving Eq. (69) for the coefficient vector $\hat{\mathbf{H}}_j \in \mathbb{R}^K$ yields the approximate solution through Eq. (65), which in turn gives the heat flux influence function

$$\Lambda_{ij} = \lambda\left(\delta_{ij} + \hat{H}_{jk}\frac{\partial \phi_k}{\partial y_i}\right). \tag{70}$$

On the macroscale, the discretization in space is performed analogously. Again, the same notation is used to refer to trial and test functions. Note, however, that the functions are defined on the macroscopic space this time, e.g., $\phi = \phi(\mathbf{x})$. Representing the temperature in the Hilbert space $\mathcal{H}_0^1(\Omega)$ with time-dependent coefficients $\hat{T} = \hat{T}(t)$

$${}^0T \approx \hat{T}_k(t)\phi_k(\mathbf{x}), \quad k = 1, \ldots, K, \tag{71}$$

and multiplying Eq. (27) by test functions $\varphi_l(\mathbf{x})$ yields

$$\begin{aligned} &\int_\Omega \overline{\rho c_p}\frac{\partial \hat{T}_k(t)}{\partial t}\phi_k(\mathbf{x})\varphi_l(\mathbf{x}) - \hat{T}_k(t)\frac{\partial}{\partial x_i}\left(\overline{\Lambda_{ij}}\frac{\partial \phi_k(\mathbf{x})}{\partial x_j}\right)\varphi_l(\mathbf{x})\mathrm{d}x = \int_\Omega \overline{Q}\varphi_l(\mathbf{x})\mathrm{d}x, \\ &\forall\, \varphi_l, \quad l = 1, \ldots, L. \end{aligned} \tag{72}$$

Henceforth, the arguments of test and trial functions are dropped for a terser notation. The second term can be rewritten using the divergence theorem and integrating the Neumann boundary condition from Eq. (27) and, therefore, it can be brought to the right side, too:

$$\int_\Omega \overline{\rho c_p}\frac{\partial \hat{T}_k(t)}{\partial t}\phi_k\varphi_l\mathrm{d}x = \int_\Omega \overline{Q}\varphi_l\mathrm{d}x + \int_{\Gamma_N} q_N\varphi_l\mathrm{d}x. \tag{73}$$

Now, the time domain is discretized using an explicit Euler scheme. Henceforth, the time step is denoted with a superscript n and the time step with Δt. With this notation in place, the temperature coefficients at the next time step $\hat{T}_k^{n+1}$ can be computed as

$$\int_\Omega \overline{\rho c_p}\hat{T}_k^{n+1}\phi_k\varphi_l \mathrm{d}x = \int_\Omega \overline{\rho c_p}\hat{T}_k^{n}\phi_k\varphi_l \mathrm{d}x + \Delta t\left(\int_\Omega \overline{Q}^n\varphi_l \mathrm{d}x + \int_{\Gamma_\mathrm{N}} q_\mathrm{N}^n\varphi_l \mathrm{d}x\right). \tag{74}$$

With the definition of the system matrix $A \in \mathbb{R}^{L\times K}$ and the thermal load vector $\mathbf{b}^n \in \mathbb{R}^L$, i.e.

$$\begin{aligned} A_{lk} &:= \int_\Omega \overline{\rho c_p}\phi_k\varphi_l \mathrm{d}x, \\ b_l^n &:= \int_\Omega \overline{\rho c_p}\hat{T}_k^n\phi_k\varphi_l \mathrm{d}x + \Delta t\left(\int_\Omega \overline{Q}^n\varphi_l \mathrm{d}x + \int_{\Gamma_N} q_N^n\varphi_l \mathrm{d}x\right), \end{aligned} \tag{75}$$

the matrix form of Eq. (74) reads

$$A\hat{\mathbf{T}}^{n+1} = \mathbf{b}^n. \tag{76}$$

3.2 *Thermo-Elastic Deformations*

In analogy to Sec. 3.1, the weak formulation is now derived for the thermo-elastic deformations. For the fine-scale problem, the test and trial functions are chosen from the same Hilbert space $\mathcal{H}_0^1(\Theta)$ of functions vanishing on the boundary. With the approximation

$${}^{mn}H \approx {}^{mn}\hat{H}_q^q\phi, \quad q = 1,\ldots,Q, \tag{77}$$

for the stress influence function, and after Eq. (62) is multiplied by test functions φ_p and integrated over the unit cell, the problem reads

$$\int_\Theta \frac{\partial}{\partial y_j}(C_{ijkl}({}^{mn}\hat{H}_q^q\phi_{(k,y_l)} + I_{klmn}))\varphi_p \mathrm{d}y = 0, \quad \forall\ \varphi_p, \quad p = 1,\ldots,P. \tag{78}$$

Applying the product identity for the divergence operator followed by the divergence theorem and taking into account the test functions vanishing on the boundary gives

$$-\int_\Theta C_{ijkl}({}^{mn}\hat{H}_q^q\phi_{(k,y_l)} + I_{klmn})\frac{\partial\varphi_p}{\partial y_j}\mathrm{d}y = 0. \tag{79}$$

The known terms can be written on the right side, which reads

$$\int_\Theta C_{ijkl}\,{}^{mn}\hat{H}_q^q\phi_{(k,y_l)}\frac{\partial\varphi_p}{\partial y_j}\mathrm{d}y = -\int_\Theta C_{ijkl}I_{klmn}\frac{\partial\varphi_p}{\partial y_j}\mathrm{d}y. \tag{80}$$

To turn this expression into matrix form, the system matrix $A \in \mathbb{R}^{P\times Q}$ and load vector $\mathbf{b} \in \mathbb{R}^P$ are defined. In coefficient notation, they read

$$\begin{aligned} A_{pq}^i &:= \int_\Theta C_{ijkl}^q\phi_{(k,y_l)}\frac{\partial\varphi_p}{\partial y_j}\mathrm{d}y, \\ {}^{mn}b^i &:= -\int_\Theta C_{ijkl}I_{klmn}\frac{\partial\varphi_p}{\partial y_j}\mathrm{d}y. \end{aligned} \tag{81}$$

With this, the matrix form

$$\mathbf{A}^i\,{}^{mn}\hat{\mathbf{H}} = {}^{mni}\mathbf{b}, \tag{82}$$

can be solved for the coefficient vector ${}^{mn}\hat{\mathbf{H}} \in \mathbb{R}^Q$.

The solution to the discretized fine-scale problem is used to define the homogenized coarse-scale material properties. First, the displacement influence function can be reconstructed using

$${}^{mn}H_i(\mathbf{y}) \approx {}^{mn}\hat{H}_q\phi_{qi}(\mathbf{y}). \tag{83}$$

Then, the strain influence function is given as

$$
\begin{aligned}
{}^{mn}E_{kl}(\mathbf{y}) &\approx I_{klmn} + {}^{mn}H_{(k,y_l)}(\mathbf{y}),\\
{}^{mn}H_{(k,y_l)}(\mathbf{y}) &= {}^{mn}\hat{H}_q \frac{1}{2}\left(\frac{\partial \phi_{qk}}{\partial y_l}(\mathbf{y}) + \frac{\partial \phi_{ql}}{\partial y_k}(\mathbf{y})\right).
\end{aligned} \tag{84}
$$

With this, and the stress influence function

$$
{}^{mn}\Sigma_{ij}(\mathbf{y}) \approx C_{ijkl}(\mathbf{y})\,{}^{mn}E_{kl}(\mathbf{y}), \tag{85}
$$

the coarse-scale stress tensor can finally be computed to

$$
{}^{\mathrm{c}}C_{ijkl} \approx \frac{1}{\mathrm{vol}(\Theta)} \int_{\Theta} {}^{mn}\Sigma_{ij}(\mathbf{y})\mathrm{d}y. \tag{86}
$$

Now, the coarse-scale stress equilibrium problem Eq. (63) is considered. Multiplying with suitable test functions $\varphi_p \in \mathcal{H}_0^1(\Omega) = \{f \in \mathcal{H}^1 | f|_{\Gamma_D} = 0\}$ and integrating over the domain Ω yields

$$
\int_{\Omega} \frac{\partial {}^{\mathrm{c}}\sigma_{ij}}{\partial x_j}\varphi_p \mathrm{d}x = -\int_{\Omega} {}^{\mathrm{c}}b_i \varphi_p \mathrm{d}x, \quad \forall\ \varphi_p, \quad p = 1, \ldots, P. \tag{87}
$$

Using, again, the product rule of the divergence operator and the divergence theorem, after inserting the traction defined on the Neumann boundary, gives

$$
\int_{\Omega} {}^{\mathrm{c}}\sigma_{ij} \frac{\partial \varphi_p}{\partial x_j}\mathrm{d}x = \int_{\Omega} {}^{\mathrm{c}}b_i \varphi_p \mathrm{d}x + \int_{\Gamma_{\mathrm{N}}} {}^{\mathrm{c}}\bar{t}_i \varphi_p \mathrm{d}x. \tag{88}
$$

Inserting the stress–strain and in turn the strain–displacement relations yields

$$
\int_{\Omega} {}^{\mathrm{c}}C_{ijkl}({}^{\mathrm{c}}\hat{u}_q^q \phi_{(k,x_l)} + \alpha \Delta {}^{\mathrm{c}}T \delta_{kl}) \frac{\partial \varphi_p}{\partial x_j}\mathrm{d}x = \int_{\Omega} {}^{\mathrm{c}}b_i \varphi_p \mathrm{d}x + \int_{\Gamma_{\mathrm{N}}} {}^{\mathrm{c}}\bar{t}_i \varphi_p \mathrm{d}x. \tag{89}
$$

Again, constant terms are brought to the right, i.e.

$$
\int_{\Omega} {}^{\mathrm{c}}C_{ijkl}\,{}^{\mathrm{c}}\hat{u}_q^q \phi_{(k,x_l)} \frac{\partial \varphi_p}{\partial x_j}\mathrm{d}x = \int_{\Omega} {}^{\mathrm{c}}b_i \varphi_p - {}^{\mathrm{c}}C_{ijkl}\alpha \Delta {}^{\mathrm{c}}T \delta_{kl} \frac{\partial \varphi_p}{\partial x_j}\mathrm{d}x + \int_{\Gamma_N} {}^{\mathrm{c}}\bar{t}_i \varphi_p \mathrm{d}x. \tag{90}
$$

Factoring out the coefficients yields

$$
\int_{\Omega} {}^{\mathrm{c}}C_{ijkl}^q \phi_{(k,x_l)} \frac{\partial \varphi_p}{\partial x_j}\mathrm{d}x\,{}^{\mathrm{c}}\hat{u}_q = \int_{\Omega} {}^{\mathrm{c}}b_i \varphi_p - {}^{\mathrm{c}}C_{ijkl}\alpha \Delta {}^{\mathrm{c}}T \delta_{kl} \frac{\partial \varphi_p}{\partial x_j}\mathrm{d}x + \int_{\Gamma_N} {}^{\mathrm{c}}\bar{t}_i \varphi_p \mathrm{d}x, \tag{91}
$$

which can be brought into the matrix form

$$
\begin{aligned}
A_i\,{}^{\mathrm{c}}\hat{\mathbf{u}} &= {}^{\mathrm{c}}\mathbf{b}_i,\\
\mathbb{R}^{P\times Q} \ni A_{ipq} &:= \int_{\Omega} {}^{\mathrm{c}}C_{ijkl}{}^{q}\phi_{(k,x_l)} \frac{\partial \varphi_p}{\partial x_j}\mathrm{d}x,\\
\mathbb{R}^{P} \ni b_{ip} &:= \int_{\Omega} {}^{\mathrm{c}}b_i \varphi_p - {}^{\mathrm{c}}C_{ijkl}\alpha \Delta {}^{\mathrm{c}}T \delta_{kl} \frac{\partial \varphi_p}{\partial x_j}\mathrm{d}x + \int_{\Gamma_{\mathrm{N}}} {}^{\mathrm{c}}\bar{t}_i \varphi_p \mathrm{d}x.
\end{aligned} \tag{92}
$$

4 From a Single Beam to Multibeam Patches

To scale up production, the laser beam can be split into multiple beams, each structuring the same cavity in parallel. This scenario can also be accounted for in the described model. The trick is to replace the periodic unit cell domain to account for a multibeam patch. Therefore, instead of the

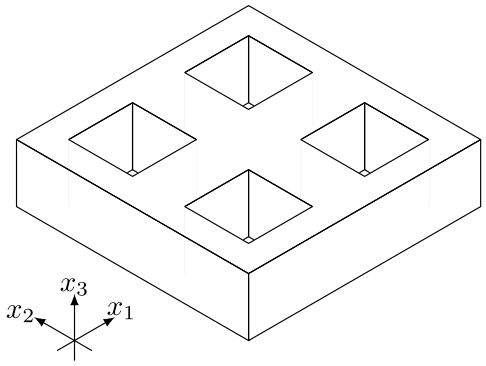

Fig. 3 A unit cell accounting for multiple holes produced by a multibeam parallel ablation process.

unit cell shown in Fig. 1(a), the unit cell consists of multiple holes ablated from a cuboid (c.f. Fig. 3). Naturally, the volume heat source, which is included in the two-scale heat conduction problem in Sec. 2.2, has to account for the multiple beams as well. In addition, the two-scale formulation is the same.

5 Numerical Experiments

To validate the two-scale model, the structuring of a foil is simulated with the multiscale approach and compared with a hole-resolved simulation.

The geometric setup is similar to the foil shown in Fig. 1(b). The foil's thickness is 2×10^{-5} m. The holes are assumed to be rectangular (c.f. Fig. 1) with a size of 4×10^{-5} m by 4×10^{-5} m on the top and a size of 2×10^{-5} m by 2×10^{-5} m on the bottom of the foil. There are 14×14 patches in the middle of the foil with 8×8 holes per patch. The holes are distributed on a patch with a hole pitch size of 5.7×10^{-5} m. This setup models a multibeam scanner unit with eight times eight laser beams (c.f. Table 1 for the beam parameters).

To structure the hole foil, a hatch strategy is needed. The scanner is set to move in the y-direction first and then in the x-direction with a speed of 0.05 m/s. For the hole-resolved simulation, each hole is discretized with a mesh of $2 \times 2 \times 1$ elements in the x, y, and z directions, respectively. On the other hand, in the multiscale simulation, the discretization is patch resolved; therefore, each patch corresponds to 1 element.

Beneath the foil, which is made of INVAR36 (c.f. Ref. 16 for the material parameters), an air layer and a soda-lime float glass layer, with a thickness of 5×10^{-6} m each, are added to dissipate heat and avoid thermally induced plastic distortions which cannot be handled by the described model. The material parameters for air and glass are shown in Tables 2 and 3, respectively.

Table 1 Laser beam.

Description	Variable
Type	Gaussian beam
Polarization	Circular
Wavelength	1×10^{-6} m
Beam radius	90×10^{-6} m
Power	100 W
Focal length	0.0 m
Rayleigh length	500 m

Table 2 Material parameters for air.

Description	Variable	Value
Poisson ratio	ν	0.156
Young's modulus	E	0.1 MPa
Thermal expansion coefficient	α	4.6×10^{-16} 1/K
Thermal conductivity	λ	0.026 W/(m K)
Specific heat capacity	c_p	1000 J/kg K
Density	ρ	1 kg/m^3

Table 3 Material parameters for soda-lime float FL glass.

Description	Variable	Value
Poisson ratio	ν	0.156
Young's modulus	E	9.1×10^4 MPa
Thermal expansion coefficient	α	4.6×10^{-6} 1/K
Thermal conductivity	λ	0.76 W/(m K)
Specific heat capacity	c_p	800 J/kg K
Density	ρ	2530 kg/m^3

It remains to define the initial conditions, the boundary conditions, and the sources. The load vectors for the microscale heat conduction problem read $\mathbf{b}_0 = (1,0,0)^T$, $\mathbf{b}_1 = (0,1,0)^T$, and $\mathbf{b}_2 = (0,0,1)^T$. For the mechanical microscale problem, the fine scale stiffness tensor has to be defined. In Voigt notation, i.e., after compressing the symmetric coefficients, the stiffness tensor can be represented as a symmetric matrix, which in turn can be stored as a vector with the entries $\mathbf{C} = (C_{11}, C_{22}, C_{33}, C_{12}, C_{23}, C_{13})$. The six load cases read $\mathbf{C}_6 = (1,0,0,0,0,0)$, $\mathbf{C}_7 = (0,1,0,0,0,0)$, $\mathbf{C}_8 = (0,0,1,0,0,0)$, $\mathbf{C}_9 = (0,0,0,1,0,0)$, $\mathbf{C}_{10} = (0,0,0,0,1,0)$, and $\mathbf{C}_{11} = (0,0,0,0,0,1)$. For the heat conduction problem, the initial condition is ambient temperature, i.e., $T_D := T_a = 298.15$ K. The Neumann boundary is chosen to be isolating on all boundaries except for the bottom one, on which a heat transition condition is set, i.e., $q_N := 10(T - T_a)$. Finally, the source is given by $Q := AP_h/(V_{\mathrm{el}} n_{\mathrm{eph}})$ with the absorption coefficient $A = 0.4$, the hole power $P_h = 0.0163416$ W, the volume of the hole $V_{\mathrm{el}} n_{\mathrm{eph}}$, and the number of elements per hole n_{eph}. For the mechanical problem, there is neither an initial condition nor a source. Instead, two boundary conditions have to be provided. The foil is clamped $u(\mathbf{x}) = (0,0,0)^T$ at $\mathbf{x} = (-1000, -1000, 0)^T$. Additionally, it is constrained in the x-direction at $\mathbf{x} = (-1000, 1000, 0)^T$ and in the y-direction at $\mathbf{x} = (1000, -1000, 0)^T$. There are no traction forces applied to the surface; therefore, ${}^{\mathrm{c}}\bar{t}_i = 0$.

To solve the time dependent system Eq. (82), the time step is chosen to yield a Courant–Friedrichs–Lewy number of $C = 1000$ and a total of 400 time steps is simulated. Then, the system is solved using the GMRES[17] algorithm and the ILU0[18] preconditioner from the PETSc project.[19] The algorithm stops when either a tolerance of 1×10^{-6} is reached or the number of iterations surpasses 100. The structural mechanics problem Eq. (92) is solved using the iterative Newton SOR method[20] with a relaxation factor of 1.5.

6 Results

The solutions to the microscale problem were computed once per load case. This information was then fed into the patch-resolved simulation. Therefore, there are no comparisons to the hole-

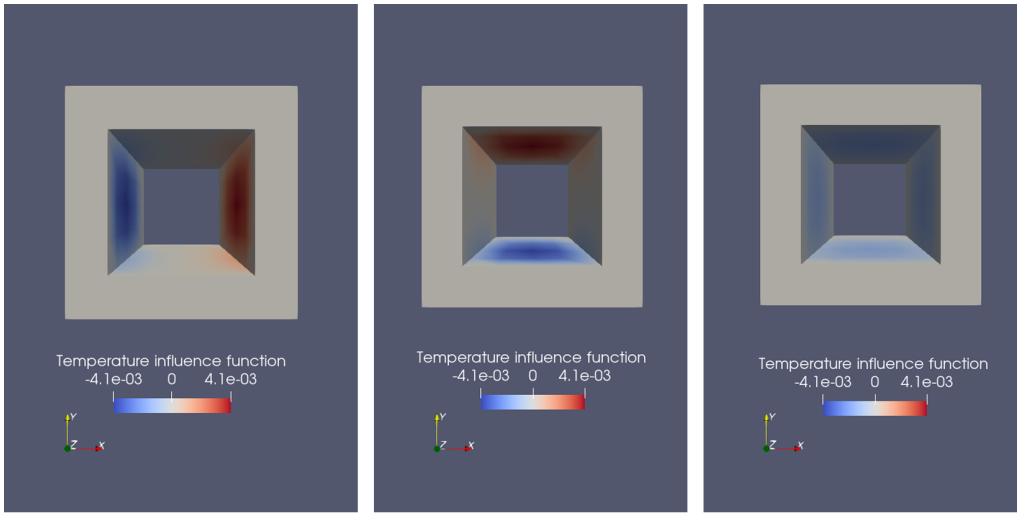

Fig. 4 The temperature influence function H_j for the three load cases $(1,0,0)^T$, $(0,1,0)^T$, and $(0,0,1)^T$ is shown in Figs. 4(a)–4(c), respectively.

resolved simulation. It can be seen that the temperature influence function depends highly on the fine scale thermal conductivity λ, which enters Eq. (26) on the right side (c.f. the left and middle pictures compared with the right one in Fig. 4).

Figure 5 shows the displacement influence function for the first three load cases. Again, it can be seen that the geometry and the stiffness tensor play the dominant role as the displacement influence function in the right most plot is not as affected as in the other two cases.

In Fig. 6, it can be seen that the temperature field is highest in the middle of the structured area. Even though the ablation area is rectangular, there is an almost radial symmetric temperature dissipation. Note, however, that the midpoint of this radial symmetric field is slightly shifted toward the right and the top of the structured area. This is an effect of the hatch strategy, which drives the laser from the lower left to the upper right corner. Because the heat cannot dissipate into the holes, the cooling rate is highest at the corners, high at the border of the pattern, and lowest at the midpoint. Hence, it is a radial symmetric temperature field.

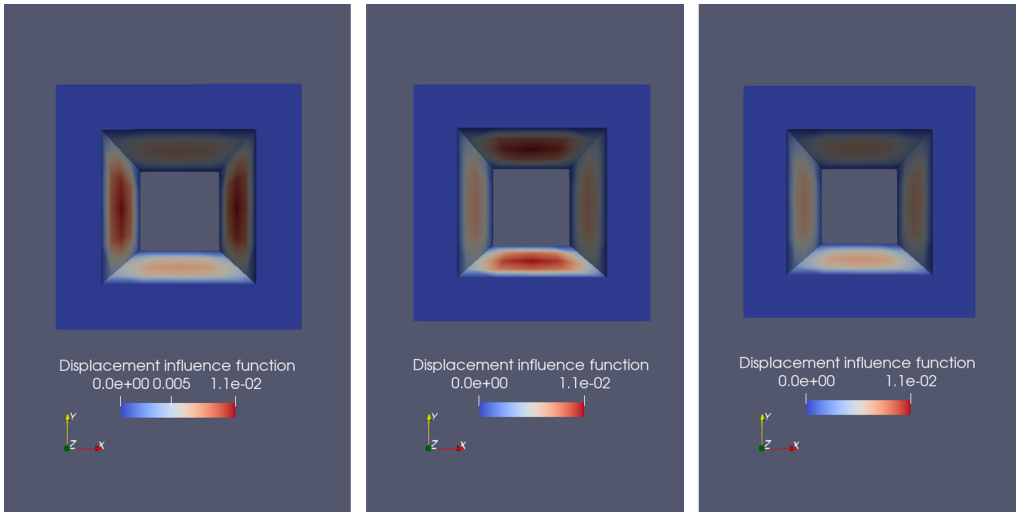

Fig. 5 The magnitude of the displacement influence function ${}^{mn}H$ for the first three (out of six) load cases, i.e., $(1,0,0,0,0,0)^T$, $(0,1,0,0,0,0)^T$, and $(0,0,1,0,0,0)^T$ is shown in Figs. 5(a)–5(c), respectively.

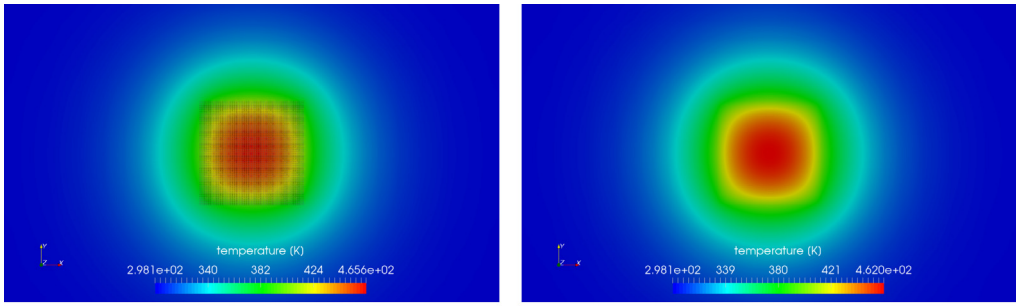

Fig. 6 The temperature of the hole-resolved simulation is displayed in Fig. 6(a) and the multiscale simulation in Fig. 6(b).

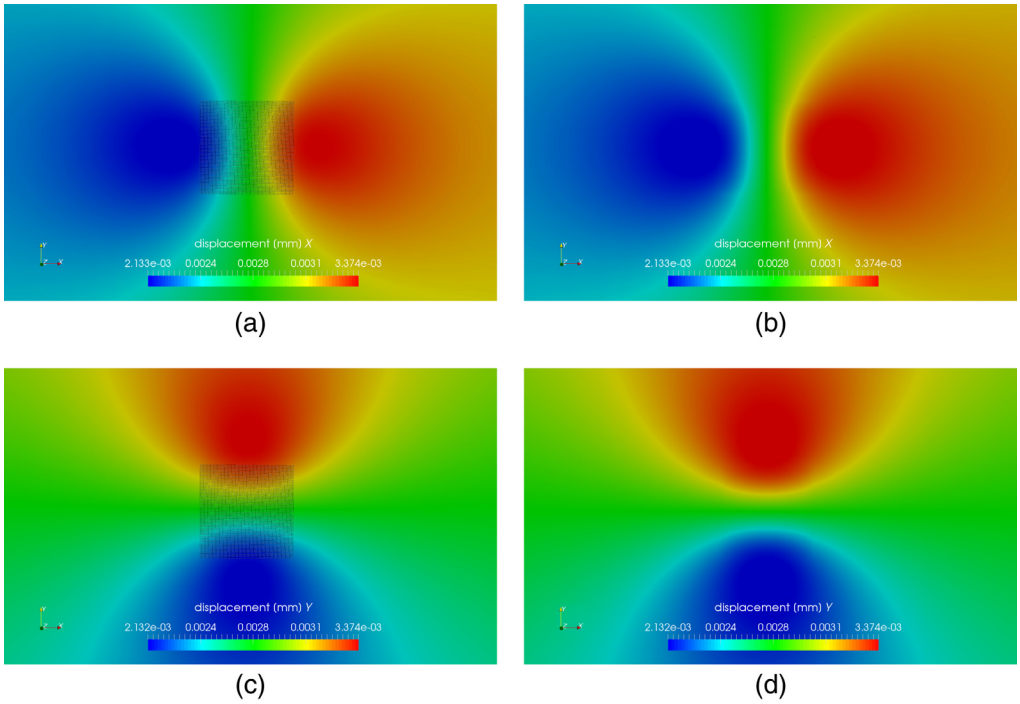

Fig. 7 The displacement of the hole-resolved simulation in the x- and y-directions [c.f. Figs. 7(a) and 7(b)] and the multiscale simulation in the x- and y-directions [c.f. Figs. 7(c) and 7(d)].

The displacements in Fig. 7 are higher in the positive x or y direction, respectively. As the deformation is solely driven by the temperature differences, this is again an impact of the hatching strategy. The elastic deformations in the left or bottom edge are already reducing to the initial configuration, whereas the deformation at the upper and right edges have just occurred. The somewhat lower displacements at the corner are a direct result of the clamping boundary conditions, which act on the bottom side of the foil.

The von Mises stresses in Fig. 8 are lower at the corners and the edges of the foil and highest in the middle. This actually visualizes the clamping conditions and explains the reduced deformations toward the corners. Because the process is temperature based, it is obvious that the von Mises stress show a similar pattern as the temperature field.

Finally, it is observed that the results of both the hole-resolved and the patch-resolved simulations coincide. The total runtime for the hole-resolved simulation was 36 067 s. The patch-resolved simulation took 421 s to compute the RVEs and 23 s to simulate the foil using the RVEs. In total, it is an improvement of over 98%, but because the RVEs only need to be computed once per material and hole shape, the improvement for further runs is even better at over 99%.

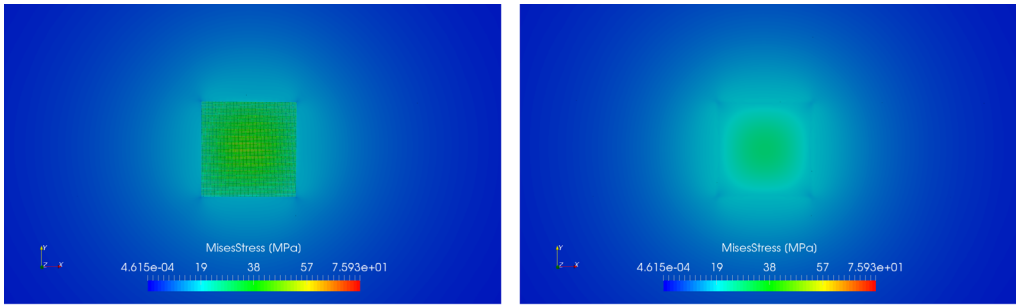

(a) (b)

Fig. 8 The von Mises stress of the hole-resolved simulation is displayed in Fig. 8(a), and the multiscale simulation is in Fig. 8(b).

7 Conclusion and Outlook

To develop the necessary process understanding to allow for a first-time-right production of FMMs, it is essential to have a fast simulation that aids in the search for better processing strategies. Therefore, a multiscale approach was developed within this treatise. This mathematical model consists of a two-scale heat conduction problem and a two-scale thermo-elasticity problem. In total, four tasks needed to be solved, two for the heat conduction and two for the structural mechanics. The discretization in space was performed using a Bubnov-Galerkin method, and the time discretization of the heat conduction problem was realized with the Euler method.

The implementation of the multiscale model is capable of reproducing the results simulated with a microscale model in a fraction of the time. The total achieved improvement in runtime is over 98% with an absolute runtime of a few seconds for the shown experiment.

The multiscale simulation enables scientists and researchers to explore and evaluate different scanning strategies with respect to the temperature-induced distortions in the work piece. Additionally, the processing strategies for filters or FMMs can be found faster compared with experiments, which might yield a quicker production ramp-up.

The current model does not account for plastic deformations. However, the yield stress is a good indicator for the occurrence of plastic deformations and can therefore be used to prevent situations in which the model fails to work. In future research, the authors plan to validate the model against physical experiments. In addition, the automation of the chain of calibrations and simulations is desired. Finally, the simulation might be used as a basis for an optimization algorithm, which selects the best scanning strategy for structuring thin foils.

Acknowledgments

Funded by the Deutsche Forschungsgemeinschaft (DFG, German Research Foundation) under Germany's Excellence Strategy—EXC-2023 Internet of Production—390621612. In addition, the authors acknowledge the publication of a prior version of this treatise in the Proceedings of the SPIE Photonics WEST 2022 conference.[21] The authors have no relevant financial interests in this manuscript and no other potential conflicts of interest to disclose.

References

1. K. Kim et al., "FMM materials and manufacturing process: review of the technical issues," *SID Symp. Dig. Tech. Pap.* **49**(1), 1011–1013 (2018).
2. C. Kim et al., "Fine metal mask material and manufacturing process for high-resolution active-matrix organic light-emitting diode displays," *J. Soc. Inf. Disp.* **28**(8), 668–679 (2020).
3. O. Hofmann et al., "Highly dynamic positioning of individual laser beams in a multi-beam system for laser surface processing," *Proc. CIRP* **94**, 812–816 (2020).

4. S. Eifel, *Effizienz- und Qualitätssteigerung bei der Lasermikrobearbeitung mit UKP-Lasern durch neue optische Systemtechnik*, 1. aufl ed., Ergebnisse aus der Lasertechnik, Apprimus (2015).
5. C. Heinigk et al., "A multi-scale model for ultra short pulsed parallel laser structuring—Part I. The micro-scale model," *J. Laser Micro Nanoeng.* **16**(2), 144–149 (2021).
6. J. Fish, *Practical Multiscaling*, John Wiley & Sons Inc. (2013).
7. J. Fish and R. Fan, "Mathematical homogenization of nonperiodic heterogeneous media subjected to large deformation transient loading," *Int. J. Numer. Methods Eng.* **76**(7), 1044–1064 (2008).
8. J. Fish, ed., *Multiscale Methods: Bridging the Scales in Science and Engineering*, Oxford University Press (2010).
9. E. Weinan, *Principles of Multiscale Modeling*, Cambridge University Press (2011).
10. W. E. B. Engquist et al., "Heterogeneous multiscale methods: a review," *Commun. Comput. Phys.* **2**(3), 367–450 (2007).
11. B. Neuenschwander, B. Jaeggi, and M. Schmid, "From fs to Sub-ns: dependence of the material removal rate on the pulse duration for metals," *Phys. Proc.* **41**, 794–801 (2013).
12. T.-R. Hsu, *Finite Element Method in Thermomechanics*, Springer Netherlands (2012).
13. A. F. Bower, *Applied Mechanics of Solids*, CRC Press (2010).
14. O. C. Zienkiewicz, R. L. Taylor, and D. Fox, *The Finite Element Method for Solid and Structural Mechanics*, 7th ed., Elsevier/Butterworth-Heinemann (2014).
15. I. Temizer, "On the asymptotic expansion treatment of two-scale finite thermoelasticity," *Int. J. Eng. Sci.* **53**, 74–84 (2012).
16. G. Hausch and H. Warlimont, "Single crystalline elastic constants of ferromagnetic face centered cubic Fe-Ni invar alloys," *Acta Metall.* **21**(4), 401–414 (1973).
17. Y. Saad and M. H. Schultz, "GMRES: a generalized minimal residual algorithm for solving nonsymmetric linear systems," *SIAM J. Sci. Stat. Comput.* **7**(3), 856–869 (1986).
18. Y. Saad, *Iterative Methods for Sparse Linear Systems*, The PSW Series in Computer Science, PWS Publ. Co (1996).
19. S. Balay et al., *PETSc/TAO Users Manual*, 7. Argonne National Laboratory, Illinois (2022).
20. D. M. Young and W. Rheinboldt, *Iterative Solution of Large Linear Systems*, Elsevier Science (2014).
21. C. Heinigk et al., "A multi-scale model for ultra short pulsed parallel laser structuring—Part II. The macro-scale model," *Proc. SPIE* **11994**, 119940B (2022).

Biographies of the authors are not available.